mater.scichina.com link.springer.com

Published online 29 September 2022 | https://doi.org/10.1007/s40843-022-2178-x
Sci China Mater 2023, 66(2): 780–792

A low-density high-entropy dual-phase alloy with hierarchical structure and exceptional specific yield strength

Yasong Li[1], Wei-Bing Liao[2*], Huaican Chen[3], Jamieson Brechtl[4], Wenli Song[3], Wen Yin[3], Zhanbing He[1], Peter K. Liaw[5] and Yong Zhang[1,6,7*]

ABSTRACT **A high-entropy dual-phase AlTiVCoNi alloy with a low density of ~6.24 g cm^{-3} is developed, and it consists of a hierarchical structure, including an ordered $L2_1$ phase, a disordered body-centered-cubic (BCC) solid-solution phase, and nano-sized $L2_1$ precipitates embedded in the BCC phase. It is found that this new alloy shows phase stability after the heat treatment at 1200°C for 24 h, and the compressive yield strength of this annealed alloy is approximately equal to that of the as-cast condition, ~1.6 GPa. This alloy displays an exceptional compressive strength at room temperature and at 600°C, with the specific yield strengths of ~261 and ~210 MPa g^{-1} cm^3, respectively. The semi-coherent interface of the $L2_1$ and the BCC phases makes the alloy phase stable and regulates the work-hardening mechanism. Local dynamic-recrystallization behavior and grain evolution are observed in the as-prepared alloy during compression at 800 and 1000°C, which results in the high-temperature softening. This alloy with a muti-phase hierarchical structure would provide a new paradigm for the development of next-generation low-density, high-entropy structural materials for high-temperature applications.**

Keywords: low-density, hierarchical structure, high-entropy alloy, $L2_1$ high-entropy intermetallic compound, specific yield strength

INTRODUCTION

The development of Ni-, Co-, and Fe-based superalloys widely used in gas turbines and aero engines has benefited to change the daily life of human beings for decades. However, to obtain more efficiency and environmental friendliness, there is an urgent demand for the development of a new generation of structural alloys with low densities and high yield strengths for high-temperature applications. Recently, high-entropy alloys (HEAs) have provided a new idea for the material design from the perspective of entropy [1–7], and many researchers have paid attention to this hot topic. Previous studies have shown that HEAs have the desirable characteristics of thermal stability, oxidation resistance, and high strengths at elevated temperatures [8–13]. Therefore, the development of low-density HEAs with excellent high-temperature properties can provide a new design idea for superalloys [14].

In terms of lightweight HEAs, the initial research mainly focused on the Al, Mg, and Li elements, which generally have relatively low densities of less than ~3 g cm^{-3} and low melting points of ~600°C [15–21]. These materials are easy to form complex intermetallic compounds rather than simple solid-solution structures. Then, by adding high melting-point elements, such as Ti, Sc, Be, and Si, the low-density HEAs with single-phase solid-solution structures have been developed, including AlLiMgScTi [22] and $Al_{20}Be_{20}Fe_{10}Si_{15}Ti_{35}$ [23]. These alloys have been reported to exhibit high specific hardness values of larger than ~2 GPa g^{-1} cm^3, and the $Al_{20}Be_{20}Fe_{10}Si_{15}Ti_{35}$ has been found to display excellent oxidation resistance at temperatures of 700–900°C. On the other hand, in terms of high-temperature applications, Senkov *et al.* [24]had developed equiatomic HEAs composed of four or five refractory metals (Mo, Nb, Ta, W, and V), and Feng *et al.* [25] had developed a single-phase CrMoNbV refractory HEA. Although these alloys exhibit outstanding high-temperature mechanical properties (far beyond Ni-based superalloys) [24,26], the inherent high density limits their wide applications.

Recently, a proper elemental selection that effectively combines lightweight metals and refractory transition metals (RTMs), based on Al-Ti-RTMs systems, appears to be a very promising way for providing a new class of materials that can overcome some intrinsic limitations found in the state-of-the-art titanium, nickel, or molybdenum alloys. Some of these alloys consist of a single-phase body-centered-cubic (BCC) structure and have a density of about ~6 g cm^{-3}, which exhibits desirable mechanical behavior [24,27–32]. The AlNbTiV HEA shows high strengths but poor plasticity at room temperature [27], while the addition of Zr in the $AlNbTiVZr_{0.5}$ can enhance its specific

[1] Beijing Advanced Innovation Center of Materials Genome Engineering, State Key Laboratory for Advanced Metals and Materials, University of Science and Technology Beijing, Beijing 100083, China
[2] Key Laboratory of Optoelectronic Devices and Systems of Ministry of Education and Guangdong Province, College of Physics and Optoelectronic Engineering, Shenzhen University, Shenzhen 518060, China
[3] Spallation Neutron Source Science Center, Institute of High Energy Physics, Chinese Academy of Sciences, Dongguan 523803, China
[4] Energy and Transportation Science Division, Oak Ridge, TN, 37831, USA
[5] Department of Materials Science and Engineering, The University of Tennessee, Knoxville, TN, 37996, USA
[6] Beijing Key Laboratory for Magneto-Photoelectrical Composite and Interface Science, University of Science and Technology Beijing, Beijing 100083, China
[7] Shunde Graduate School of University of Science and Technology Beijing, Foshan 528399, China
* Corresponding authors (emails: drzhangy@ustb.edu.cn (Zhang Y); liaowb@szu.edu.cn (Liao WB))

strength and plasticity [28]. Another study found that $Ti_{50-x}Al_xVNbMo$ HEAs have high compressive strength and good plasticity, compared with typical Ni-based superalloys, and it was also reported that adding Al to the HEA can enhance its strength [29]. Moreover, other low-density HEAs exhibiting single BCC structures, such as AlTiCr(V,Zr,Nb) [30–32], $Al_2NbTi_3V_2Zr$ [33], $Ti_3V_2NbAl_xNi_y$ [34], and $Ti_{1.5}ZrNbAl_{0.3}$ [35], have also been developed, and these alloys can indeed achieve excellent high-temperature strengths.

However, some studies have reported that the mechanical properties of low-density HEAs can be further improved by regulating the multi-phase structure [8,9,36–39]. For instance, Senkov *et al.* [36] investigated low-density Cr-Nb-Ti-V-Zr HEAs systems, which found that with the addition of Cr, the structure changed from disordered-BCC phases to BCC + Laves structures, and their high-temperature (600–1000°C) yield strengths were significantly improved with the ordered Laves phase [37]. Feng *et al.* [38] investigated the effects of the Al/Ti addition on mechanical properties of $Al_xCrFeMnTi_y$ HEAs with the BCC + $L2_1$ + Laves structure, and their subsequent studies on the $Al_{1.5}CrFeMnTi$ HEA further reported that the multi-phase structural transformation could be controlled by a suitable heat treatment to achieve the desired material performance [39]. Moreover, $Al_{20}Cr_5Fe_{50}Mn_{20}Ti_5$ and $AlCr_{1.3}TiNi_2$ dual-phase HEAs with multi-phase structures have been developed by Feng *et al.* [8] and Wang *et al.* [9], respectively, and they all exhibited good mechanical properties at elevated temperatures. That is to say, these multiphase HEAs exhibit higher yield strengths and better high-temperature properties, as compared with those of single phase HEAs.

It is thought that the design of a muti-phase structure can potentially enhance the desirable properties by adding some new strengthening mechanism, such as precipitation strength. In this study, a new low-density (~6.24 g cm^{-3}) AlTiVCoNi HEA with the dual-phase hierarchical structure was developed. It contained a novel and hard ordered-$L2_1$ high-entropy intermetallic compound (HEIC) phase, a soft BCC solid-solution phase, and a nano-size $L2_1$ HEIC phase, which makes it exhibit excellent elevated-temperature phase stability and strength. We characterized the microstructure of this alloy in detail and studied its strengthening mechanism and high-temperature softening mechanism.

EXPERIMENTAL SECTION

Sample preparation

The equiatomic AlTiVCoNi HEA ingot was synthesized by argon-protected arc-melting, using a mixture of the metallic elements (purity > 99.95 wt%). The ingot was re-melted 5 times and eventually suction-cast with a copper mold (10 mm × 10 mm × 40 mm). Then some of the alloy ingots were heat-treated at 1200°C for 24 h under the condition of a closed vacuum quartz tube, which was followed by water quenching. Samples for compression tests were cut from the ingot along the length direction, with a size of Φ3 mm × 6 mm.

Microstructure characterizations

Microstructures and morphologies were characterized by Zeiss Supra 55 and Zeiss Genimi 450 field emission scanning electron microscope (SEM), equipped with an energy-dispersive X-ray spectrometer (EDS) and the electron backscattered diffraction (EBSD), to realize the separation of $L2_1$ and BCC phases by means of the combined EDS and EBSD method. The EBSD samples were prepared with a mechanical polishing machine, using the ChemoMet™ oxide-polishing cloth and MasterMet™ silicon-dioxide suspension of 0.02 μm for 1 h. The standard bright-field (BF), dark-field (DF) images and selected area electron diffraction (SAED) patterns were obtained by a transmission electron microscope (TEM, Tecnai F30) operated at 300 kV, and the TEM data processing adopted Digital Micrograph software. The X-ray diffraction (XRD) was conducted, employing the Rigaku Smart Lab, 9 kW, 45 kV, with Cu Kα radiation. Here, scattering angles in the range of 20°–90° and a scanning rate of 5° min^{-1} were used. The neutron-scattering measurements were performed to identify the detailed phase structure of the AlTiVCoNi alloy on the multiple physics instrument (MPI) with a Q range of 1–50 A^{-1}, at China Spallation Neutron Source (CSNS) [40]. The detectors, which were divided into 5 banks (Bank 3–Bank 7), were calibrated, using a National Institute of Standards and Technology (NIST) silicon powder standard prior to the measurements. During testing, the samples with a size of Φ9 mm × 10 mm were put into the ZrTi cell and measured at room temperature for 0.5 h, with a scattering chamber pressure of ~10^{-4} Pa. The empty ZrTi cell, a V rod, and background data were obtained for the data reduction and correction, using the program Mantid. Five neutron-diffraction patterns from Banks 3–7 were obtained, respectively, and the data from Bank 6 were used. The chemical concentration of the sample was investigated, employing the local electrode atom probe tomography (APT, LEAP 5000×SI), and the sharp APT tip was prepared by the conventional focused ion beam (FIB, Thermo Scientific™ Helios G4 CX Dual Beam) milling process.

The density of the alloy was measured *via* the Archimedes Principle [41]. The measurement formula is described as follows [42]:

$$\rho_{\text{measured}} = \frac{m_1}{m_2}\rho_{H_2O}, \quad (1)$$

where ρ_{measured} is the measured density of the alloy, m_1 is the mass of the sample in air, m_2 is the mass gain of the water with the sample immersed in distilled water, and ρ_{H_2O} is the density of water.

Mechanical tests

Room-temperature compression tests were conducted by a CMT4105 universal electronic testing machine with an initial strain rate of 1.0 × 10^{-3} s^{-1}. Additionally, high-temperature compression properties were studied, employing a Gleeble1500 thermal simulation testing machine at temperatures of 600, 800, and 1000°C with a strain rate of 1.0 × 10^{-3} s^{-1} in air. Three samples were tested at each temperature. To characterize the hardness and elastic modulus of the samples, nanoindentations were carried out, using an MTS Nano Indenter II with a Berkovich triangular pyramid indenter containing a tip radius of 20 nm, with the Poisson's ratio of 0.33 [43]. Five indents were performed to a depth of ~2000 nm for the average nano-hardness. Furthermore, twenty five points were performed to a depth of 500 nm with the distance of 10 μm in order to distinguish the hardness of different phase structures. The indentation morphology was presented in Fig. S1. Micro-hardness measurements were obtained by a Wolpert-401MVD Vickers hardness tester,

using a pyramid indenter with a 200 g load and dwell time of 15 s.

RESULTS

Alloy design

In view of the concept of HEAs, we expect to design and develop a new alloy with low density and high yield strength for high-temperature applications. Firstly, the density of the superalloy is expected to be reduced. Hence, two low-density elements, Al and Ti, are chosen to be added to the Co-Ni system. However, as Al or Ti has a negative binary mixing enthalpy (ΔH_{mix}) (≤ -20 kJ mol^{-1}) with other elements, it is easy for the alloy to form intermetallic phases. The binary mixing enthalpy of the refractory low-density element, V, with these four elements is found to be relatively high (≥ -20 kJ mol^{-1}). Therefore, we designed to add V to the Co-Ni-Al-Ti alloy to form the solid solution phase. Thus, the alloy can form a muti-phase structure of HEICs and solid solutions. Fig. 1 shows the binary ΔH_{mix} between these added elements [44]. It can be determined from the figure that the mixing enthalpy between Co and Ni was 0, and the mixing enthalpy between the other elements was relatively negative. The formation rules of HEA phases [1,45–49], such as $\Delta H_{mix} \sim \delta$ (atomic-radius difference), and Ω (a multi-component solid-solution criterion), are used in this study to design the phase structures of this lightweight alloy. The criteria were mainly based on ΔS_{mix}, ΔH_{mix}, δ, and T_m, as defined by the following equations:

$$\Delta H_{mix} = \sum_{i=1, i\neq j}^{n} 4c_i c_j \Delta H_{mix}^{ij}, \quad (2)$$

$$\delta = \sqrt{\sum_{i=1}^{n} c_i \left(1 - \frac{r_i}{\sum_{i=1}^{n} c_i r_i}\right)^2}, \quad (3)$$

$$\Delta S_{mix} = -R \sum_{i}^{n} c_i \ln c_i, \quad (4)$$

$$\Omega = \left| T_m \Delta S_{mix} / \Delta H_{mix} \right|, \quad (5)$$

where ΔH_{mix}^{ij} denotes the mixing enthalpy of the ith and jth elements, c_i and c_j are the compositions of the ith and jth elements, r_i is the atomic radius of the ith element, respectively, R is the gas constant, and T_m is the average melting point. Through calculations, we know that ΔH_{mix} is ~−29.44 kJ mol^{-1}, δ is ~6.35%, ΔS_{mix} is 1.61R, and T_m is ~1709 K. Moreover, it is determined that Ω is ~0.78, which is less than 1.1. The entropy and enthalpy in a system present a balance point, which is at the boundary regions of the phase-formation ruler map. Thus, according to the corresponding criteria, the designed alloy will tend to form a multiphase structure.

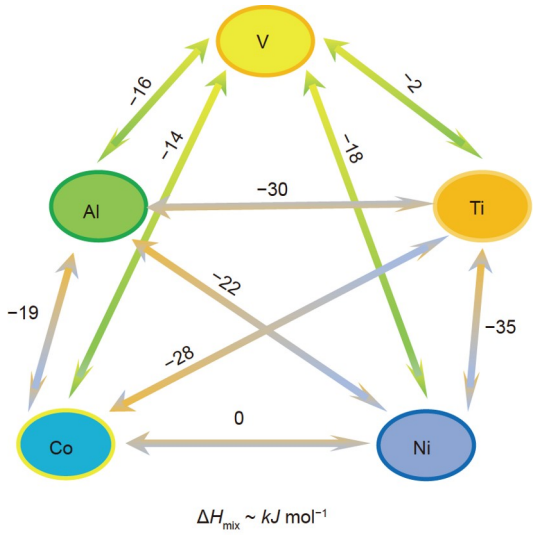

Figure 1 Binary mixing enthalpy between each constituent element in the AlTiVCoNi HEA.

Phase structure and phase stability

Fig. 2a presents the XRD patterns of the as-cast and annealed AlTiVCoNi alloys. It is found that this alloy shows a multi-phase structural feature, which coincides well with our initial design goal. Also, the phases in the as-cast alloy are identified to be an ordered-L2$_1$ (each atom in the fixed site in the lattice) and a disordered-BCC solid solution crystalline structure. To further identify the phase structure of this alloy, the neutron-scattering measurements were performed on both the as-cast and annealed samples, presented in Fig. 2b, the ordered-L2$_1$ and BCC phases were confirmed. With the Rietveld refinements on the neutron-

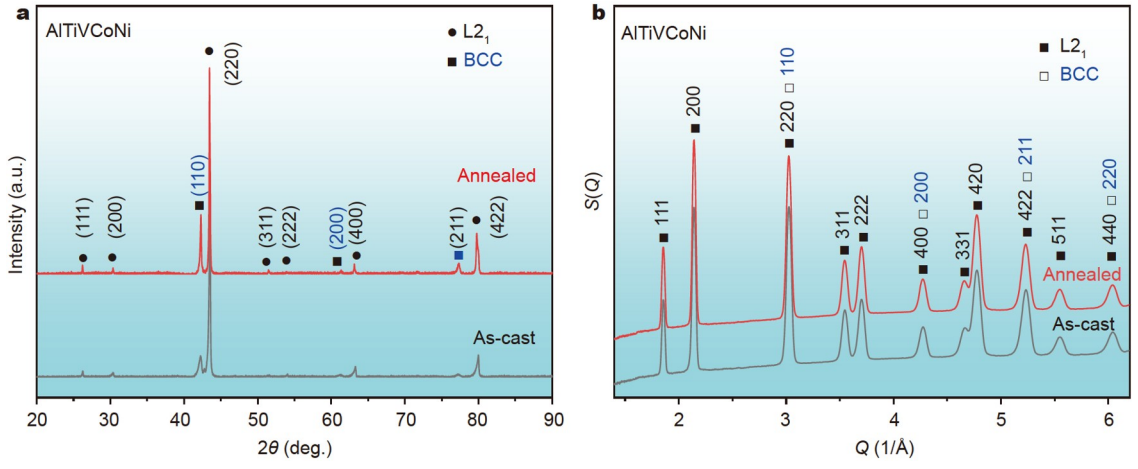

Figure 2 The phase structure of the AlTiVCoNi HEA: (a) the XRD patterns of the as-cast and annealed (1200°C + 24 h) samples; (b) the neutron-diffraction patterns of the as-cast and annealed samples.

diffraction results by the GSAS-Ⅱ software, the lattice parameters of this alloy were calculated, and the lattice constants of the $L2_1$ and BCC phases were determined to be 5.879 and 2.943 Å, respectively. After annealing at 1200°C for 24 h, no other phases appeared in the alloy, indicating that this developed alloy has the phase stability under the prescribed high-temperature condition, as shown in Fig. S2. Due to the high-entropy effect, the concentration of constituent atoms with different intrinsic properties (including atomic sizes, bonds, activity, and electronegativity) is high. In this case, the diffusion of atoms at high temperatures is subject to complex interactions, and the diffusion is therefore hindered [50–52]. It has been reported that the as-prepared HEICs are phase stable and indicate an efficient approach for enhancing the alloy strength [53]. Hence, it could provide a basic support for the high-temperature application of this alloy.

Microstructures

The SEM micrograph of the as-cast AlTiVCoNi alloy is shown in Fig. 3a. The alloy exhibits two distinct structural regions: a gray matrix phase (GMP) region, and a dark gray phase (DGP) region. The EDS analyses reveal that the V content in the alloy is ~22 at%, while the amount of the other elements is approximately in an equal ratio, ~19 at%. This trend is mainly due to the relatively high melting point of V that leads to less burnout during smelting. Interestingly, the distribution of the Al, Ti, and Co elements in the matrix GMP region is uniform (~20 at%), and the Ni content is a bit higher (~28 at%), while there is a relatively small amount of V (~6 at%). With the data of the EDS test, we calculated the mixing entropy, ΔS_{mix}, of the GMP, which is ~1.51*R*, indicating that the ordered-$L2_1$ phase is an HEIC. On the other hand, the DGP region contains a V-rich BCC solid-solution phase, which is similar to that of a typical vanadium alloy lattice structure, as presented in Fig. 2, and it is further determined by subsequent TEM analyses. The chemical compositions of the GMP and DGP in the as-cast sample are almost the same as those in the annealed sample. The results of the EDS characterization are presented in Table 1. Fig. 3b displays the

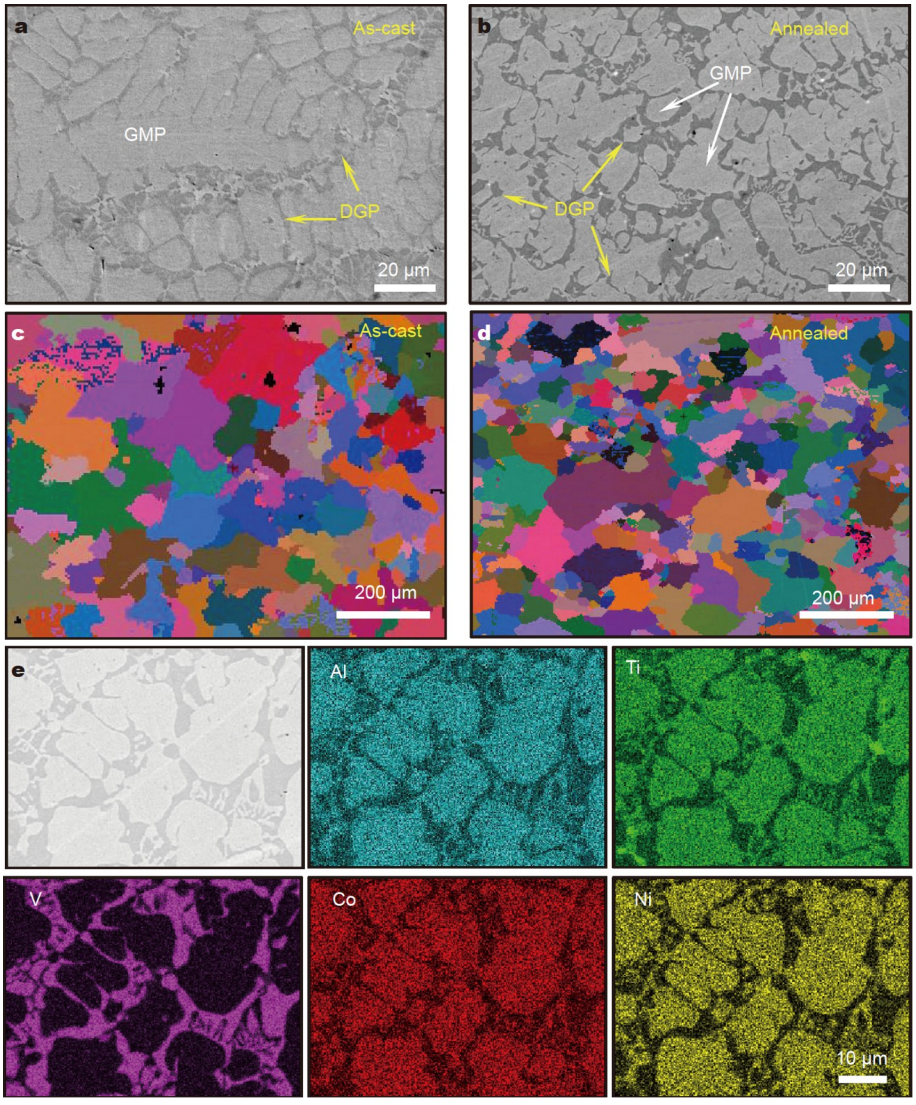

Figure 3 SEM photographs and elemental-composition mappings of the AlTiVCoNi alloy (15 kV): (a) the secondary electron image of the as-cast sample; (b) the BSE image of the sample annealed at 1200°C for 24 h, where the GMP consists of a high-entropy intermetallic structure consisting of the $L2_1$ phase, and DGP is the V-rich phase with a BCC structure; (c, d) the EBSD images for the as-cast and the annealed samples; (e) the elemental mapping of the annealed alloy.

Table 1 The composition and EDS analysis results of the AlTiVCoNi HEAs (C: as-cast, A: annealed)

Composition (at%)	Al	Ti	V	Co	Ni
Nominal	20	20	20	20	20
Actual	18.91 ± 0.13	19.79 ± 0.17	22.22 ± 0.19	19.50 ± 0.31	19.58 ± 0.38
GMP-C	22.98 ± 0.10	20.38 ± 0.11	5.87 ± 0.07	22.07 ± 0.17	28.67 ± 0.14
DGP-C	5.84 ± 0.05	7.90 ± 0.08	73.15 ± 0.25	10.34 ± 0.13	2.75 ± 0.14
GMP-A	22.36 ± 0.10	21.56 ± 0.10	6.02 ± 0.14	24.00 ± 0.12	26.06 ± 0.21
DGP-A	5.31 ± 0.37	7.96 ± 0.75	72.75 ± 1.25	10.52 ± 0.19	3.46 ± 0.11

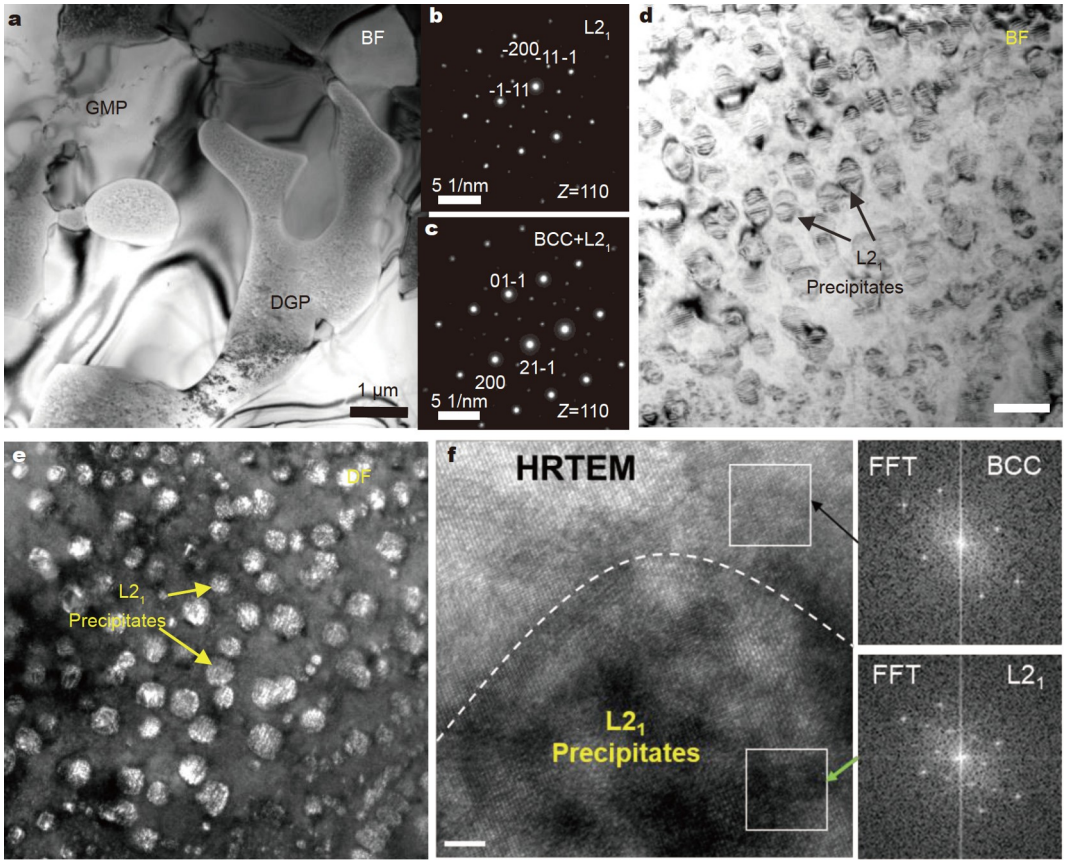

Figure 4 (a) TEM BF phase of the as-cast AlTiVCoNi alloy, (b, c) SAED patterns of GMP and DGP, (d, e) the BF and the DF enlarged view images of DGP, and (f) the HRTEM image of the nano-$L2_1$ precipitates and the BCC solid solution in DGP. The scale bars of (d–f) are 100, 100, and 2 nm, respectively.

back-scattered electron (BSE) photograph of the sample that was annealed at 1200°C for 24 h. The BSE image suggests that annealing at the above condition did not significantly change the phase morphology of the alloy. Fig. 3c, d present the EBSD images of the as-cast and annealed alloy samples. The results reveal that the grain structure of the as-cast sample consists of a uniform distribution of randomly oriented fine grains with an average size of ~70 μm. Furthermore, there was no observable change in the grain size and orientation after annealing, as shown in Fig. S3, which also shows that the alloy has excellent high-temperature stability. Since the size of the DGP region is on the order of several micrometers, after the phases were distinguished by the phase-separation method during the processing of the EBSD data, it can be concluded that each grain contains both the GMP and DGP structural regions (Fig. S4a). From the elemental-composition mappings shown in Fig. 3e, it can be seen that the DGP is the V-enriched region, while the GMP is primarily within the V-poor region. This alloy contains the dendrite and interdendritic regions resulting from the effect of the enthalpy of the mixing and melting-point difference. Statistics on the phase content indicate that the total area of the GMP region is ~71.17%, and the DGP region is ~28.83% in the alloy (Fig. S4b).

Then, we studied the atomic-scale microstructures in detail using TEM. It is further indicated that there are two phases in this alloy, namely the GMP and DGP, as presented in Fig. 4a. The corresponding SAED patterns are shown in Fig. 4b, c. The GMP is identified to be an oredered-$L2_1$ structure, which is an HEIC, and the DGP has a BCC + nano-$L2_1$ precipitate structure, indicating that the alloy has a hierarchical structure. Fig. 4d, e show the enlarged BF and DF images of the DGP region, and there are a large number of nano-$L2_1$ precipitates embedded in it. Fig. 4f further shows the high-resolution TEM (HRTEM) and the fast Fourier transform (FFT) images of the nano-$L2_1$ pre-

cipitates, and it suggests that there is a semi-coherent interface between the BCC and nano-$L2_1$ precipitates, where the crystal lattice constant of the nano-$L2_1$ precipitates is about twice that of the disordered BCC phase, which is consistent with the neutron diffraction results, as shown in Fig. 2b.

We further analyzed the chemical compositions and elemental distributions of the BCC and oredered-$L2_1$ phases using three-dimensional APT (3D-APT), as shown in Fig. 5. Fig. 5a presents the 3D atomic-reconstruction diagram, and it can be found that the DGP is a V-rich phase with nano-$L2_1$ precipitate phases. Fig. 5b shows the equal concentration surface with 14 at% of Al. It can be intuitively found that there are a large number of nano-$L2_1$ precipitates in the BCC solid-solution phase. With the increase of the size of the precipitates, their shape changes from spherical to cubic. Fig. 5c shows the chemical compositions of the BCC and $L2_1$ phases. The BCC phase in the alloy is mainly the V-rich phase. The Al, Ti, Co, and Ni elements' contents of the $L2_1$ phase are of approximately equal atomic ratios.

Mechanical properties

The nanoindentation test results indicate that the average nanohardness and elastic modulus of the as-cast AlTiVCoNi HEA are 7.99 ± 0.15 GPa and 209.60 ± 2.48 GPa, respectively. The elastic modulus value is similar to that of the INCONEL 718 superalloy (~204 GPa) [14], and it is almost twice that of the Ti-6Al-4V alloy (~110 GPa) [54]. It is also found that the nanohardness of the ordered-$L2_1$ phase is 9.71 ± 0.10 GPa, which is much higher than that of the area containing both the BCC solid solution and nano-$L2_1$ phase (3.38 ± 0.13 GPa), indicating that the BCC phase is a soft phase. This result also further demonstrates that the as-prepared alloy has a dual-phase structure: a hard ordered-$L2_1$ phase and a soft BCC phase. Lastly, the average Vickers hardness is 688.8 ± 4.84 $HV_{0.2}$, which is a bit smaller than the nanoindentation hardness.

The compressive engineering stress-strain curves for the as-cast and annealed AlTiVCoNi HEA samples are presented in Fig. 6a. The results indicate that the compressive yield strengths of the as-cast and annealed samples are almost at the same level, ~1.6 GPa. The elastic modulus of the AlTiVCoNi HEA, calculated by the stress-strain curve, is about 180 GPa. Moreover, the elastic deformation region of the stress-strain curves appears to overlap, suggesting that the structural and mechanical performance of the alloy remain relatively stable after high-temperature annealing. The fracture strength of the as-cast and annealed alloy is ~2.9 and ~2.6 GPa at room temperature, respectively, with a compressive plasticity of ~12%. Compared with the $Fe_{0.75}Co_{0.75}Ni_{0.75}Cu_{0.75}TiZrHf$ HEICs [55], this developed dual-phase HEA not only shows a lower density and comparable fracture strength, but also exhibits a better room-temperature plasticity (~13%). In addition, these results further verify that the alloy has structural and performance stability under high-temperature conditions. Therefore, subsequent high-temperature performance tests were conducted with the annealed samples.

The compressive engineering stress-strain curves of the annealed AlTiVCoNi HEAs compressed at 600, 800, and 1000°C are shown in Fig. 6b. As the temperature increases, the yield

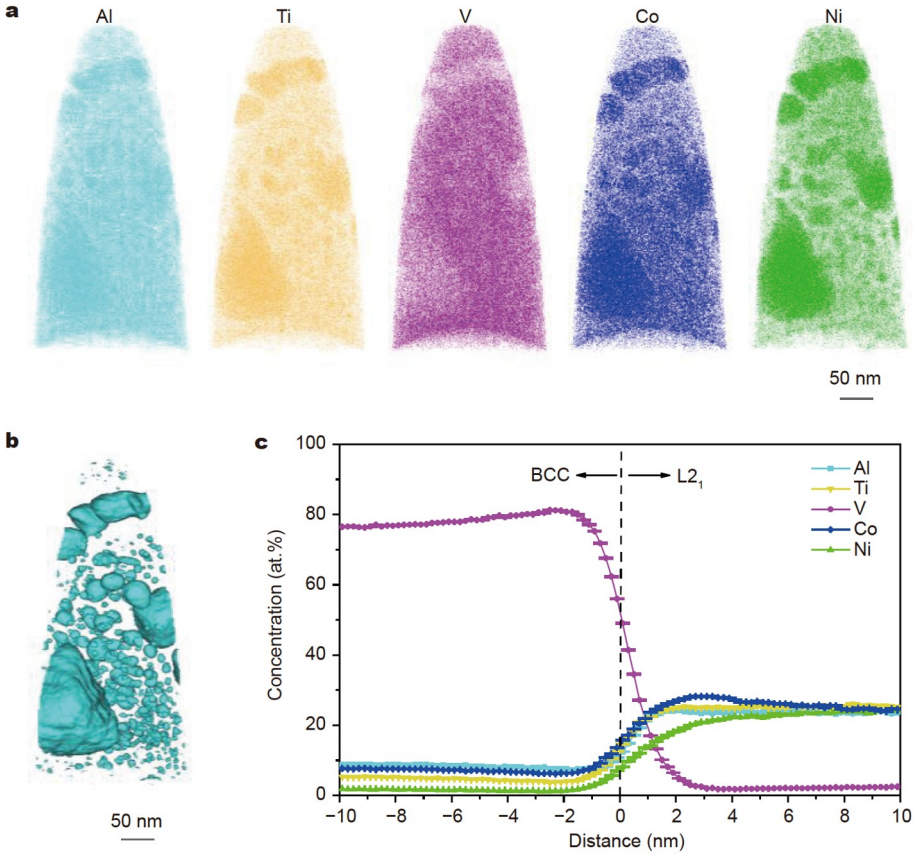

Figure 5 The 3D-APT image of the AlTiVCoNi alloy with GMP: (a) The 3D atomic-reconstruction diagram, (b) the equal concentration surface with 14 at% of Al, and (c) the chemical compositions of the BCC and $L2_1$ phases.

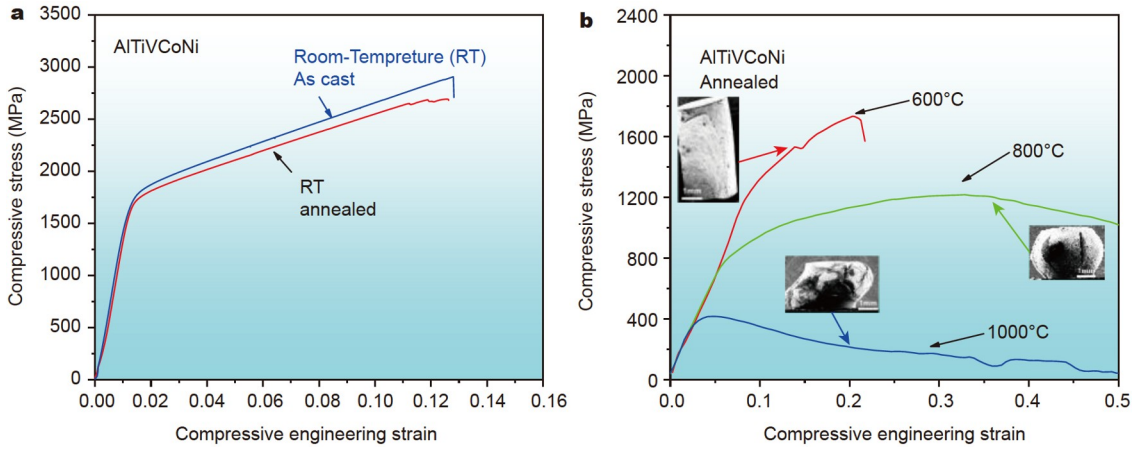

Figure 6 (a) The room-temperature compressive stress-strain curves for the as-cast and annealed samples (1200°C for 24 h). (b) The high-temperature compression performance (600, 800, and 1000°C) with the annealed compressed sample morphologies featured in the inset.

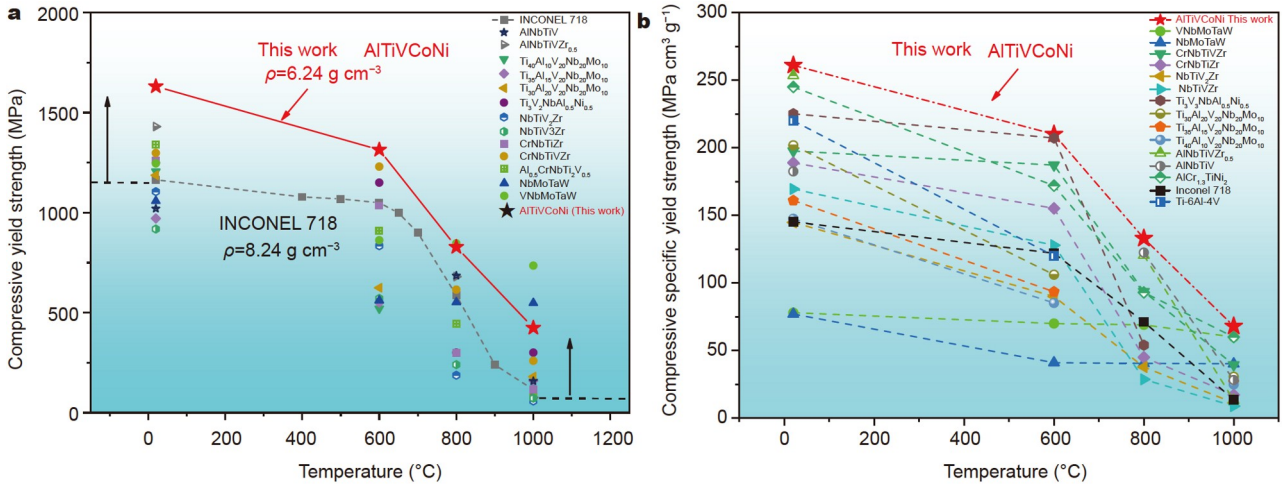

Figure 7 The comparison of mechanical performance of different alloys: (a) the high-temperature compressive yield strength *vs.* temperature; (b) the compressive specific yield strength *vs.* temperature.

strength decreases. It is noted that at 600°C, this alloy retains a high compressive yield strength of ~1.3 GPa without softening. At 800°C, the highest strength of the alloy still exceeds ~1.1 GPa, while the yield strength is ~0.8 GPa. However, the alloy exhibits softening at 1000°C, and its yield strength decreases to ~0.4 GPa. The compressed morphologies of these three samples are displayed in the inset of Fig. 6b. In contrast, the shape of the annealed samples tested at 800 and 1000°C are rounded with a drum shape. This result indicates that the plasticity of the alloy is enhanced above a certain threshold temperature. There are some fluctuations in the curves, which means that some serration behaviors happened during the high-temperature compressive testing. Due to the recrystallization in the high-temperature compression, the energy accumulation and avalanche occur at elevated temperatures, and this kind of plastic flows results in the generation of the serration behavior [56].

DISCUSSION

The comparison of different alloys' performance

Fig. 7a shows the compressive yield strength *versus* temperature relationship between the traditional superalloys (INCONEL 718) and some previously reported low-density HEAs. From the results, it is apparent that the AlTiVCoNi alloy has exceptional elevated-temperature properties, as compared with traditional superalloys and some existing low-density HEAs. It is noted that the compressive yield strength of most low-density HEAs at 1000°C is higher than that of Ni-based superalloys (INCONEL 718). Fig. 7b shows the compressive specific yield strengths of the developed AlTiVCoNi alloy and other alloys at different temperatures. The specific yield strength of the developed AlTiVCoNi alloy exceeds 260 MPa cm^3 g^{-1} at room temperature. In addition, at 600°C, the compressive specific yield strength of this alloy remains at the highest level of the investigated alloys, which exceeds 210 MPa cm^3 g^{-1}. With an increase in the temperature, the specific yield strength of this alloy is reduced. However, it remains at relatively high values of 132 and 68 MPa cm^3 g^{-1} at 800 and 1000°C, respectively. The corresponding data are shown in Table 2. Moreover, the compressive yield strengths of this alloy at 600 and 800°C are higher than those of refractory NbMoTaW HEAs (561 and 552 MPa) [24]. Furthermore, the currently investigated HEA (~6.24 g cm^{-3}) has a lower density, as compared with the above alloy (the theoretical density of NbMoTaW is ~13.61 g cm^{-3} [57]). The lower

Table 2 Density and compressive $\sigma_{0.2}$ values for some low-density HEAs, INCONEL 718, and NbMoTaW, VNbMoTaW refractory HEAs at temperatures ranging from 20 to 1000°C

Alloys	Density (g cm^{-3})	$\sigma_{0.2}$ at different temperatures (MPa)				Ref.
		20°C	600°C	800°C	1000°C	
AlTiVCoNi	6.24	1631	1314	828	424	This work
INCONEL 718	8.24	1197	1005	587	112	[14]
AlNbTiV	5.59	1020	–	685	158	[27]
$AlNbTiVZr_{0.5}$	5.64	1430	–	680	75	[28]
$Ti_{40}Al_{10}V_{20}Nb_{20}Mo_{10}$	6.1	900	520	–	155	[29]
$Ti_{35}Al_{15}V_{20}Nb_{20}Mo_{10}$	6.027	971	550	–	160	
$Ti_{30}Al_{20}V_{20}Nb_{20}Mo_{10}$	5.876	1187	624	–	180	
$Ti_3V_2NbAl_{0.5}Ni_{0.5}$	5.55	1250	1150	300	–	[34]
NbTiVZr	6.52	1105	834	187	58	[37]
$NbTiV_2Zr$	6.34	918	571	240	72	
CrNbTiZr	6.67	1260	1035	300	115	
CrNbTiVZr	6.57	1298	1230	615	259	
$Al_{0.5}CrNbTi_2V_{0.5}$	6.43	1340	910	445	90	[58]
NbMoTaW	13.61[a]	1058	561	552	548	[24]
VNbMoTaW	12.33[a]	1246	862	846	735	

a) The theoretical density of alloys with the same compositions using the rule of mixtures, $\rho_{\text{theoretical}} = \sum_{i=1}^{n} c_i A_i / \sum_{i=1}^{n} \frac{c_i A_i}{\rho_i}$ [57], where c_i, A_i, and ρ_i are the concentration, atomic weight, and density of the ith element, respectively.

density of this alloy corresponds to a 24% weight reduction, relative to traditional superalloys (INCONEL 718, a density of ~8.24 g cm^{-3}) [14]. This combination of the relatively low density, phase stability, and exceptional compressive specific yield strength makes the AlTiVCoNi HEA a potential candidate for high-temperature applications.

It is worth mentioning that there is a temperature-dependent strength of the materials with high-temperature applications. Steingrimsson *et al.* [59] proposed a break temperature (T_{break}) for predicting the high-temperature strengths in BCC HEAs, using the relationship between the strength and temperature in BCC HEAs. Steingrimsson *et al.*'s model [59] is for the ultimate strength. His model is extended to the prediction of yield strengths, as described below. This bilinear log model, which consists of a temperature-dependent yield strength, $YS(T)$, and melting temperature, T_s, is parametrized as follows:

$$YS(T) = \min(\log(YS_1(T)), \log(YS_1(T))), \quad (6)$$

$$YS_1(T) = \exp(-C_1 \times T/T_s + C_2), \ (0 \le T \le T_{\text{break}}) \quad (7)$$

$$YS_2(T) = \exp(-C_3 \times T/T_s + C_4), \ (T_{\text{break}} \le T \le T_s) \quad (8)$$

and a continuity constraint between the low-temperature and the high-temperature regimes:

$$YS_2(T) = YS_1(T), \quad (9)$$

$$T_{\text{break}} = \frac{C_4 - C_2}{C_3 - C_1} T_s, \quad (10)$$

where $\log(YS(T))$ is the common logarithm for the yield strength, and T_s is the theoretical melting point with Degrees Celsius. A conceptually simple approach is proposed for fitting the model in Equations (6–10) to the $YS(T)$ data of the AlTiVCoNi alloy. It consists of the first deriving constant. Here, the C_1 and C_2 are obtained by applying linear regression to data points at lower temperatures (room temperature, 600 and 800°C). The C_3 and C_4 are obtained by applying linear regression to data points at higher temperatures (600, 800, and 1000°C). Fig. 8 shows the results of the linear regression, where the T_{break}/T_s is found to be 0.491 for this HEA. As the T_s of this alloy is about 1436°C, the T_{break} of this HEA is approximately 700°C. Thus, it is believed that the application temperature of this alloy could exceed 700°C.

Strengthening mechanism

The schematic diagram of the strengthening mechanism in this AlTiCoNiV HEA is presented in Fig. 9. Based on the aforementioned observations, it can be seen that this developed alloy exhibits a unique hierarchical structure consisting of an ordered-$L2_1$ HEIC and disordered-BCC solid solution with semi-coherent interfaces, and a nano-sized $L2_1$ precipitates, which is significantly distinctive to conventional lightweight HEAs. The semi-coherent interfaces (which consist of the disordered and ordered phases) could produce a local high strain energy region that hinders dislocation motion, thereby increasing the strength of this HEA. With the dual-phase structure in the alloy, the semi-coherent relationship [60] between the two phases can restrict structural coarsening, when the sample undergoes deformation or is under high-temperature conditions. Also, these conditions can activate related strengthening mechanisms, which significantly improves the intrinsic yield strength of the alloy. On the other hand, the alloy primarily consists of the harder ordered-$L2_1$ phase (~71.17% in the volume fraction), making it harder as compared with conventional lightweight HEAs. In addition, the alloy contains nano-$L2_1$ precipitates in the BCC phase, which turns into the hierarchical structure, also contributing to its high strength. Due to the synergistic effect of the large and nanoscale-sized $L2_1$ phases, dislocation motion can be effectively hindered during deformation. These hierarchical structures therefore lead to its outstanding service performance at room temperature and 600°C. Similarly, adjusting the amount

of hierarchical structures can be a useful design strategy for low-density HEAs.

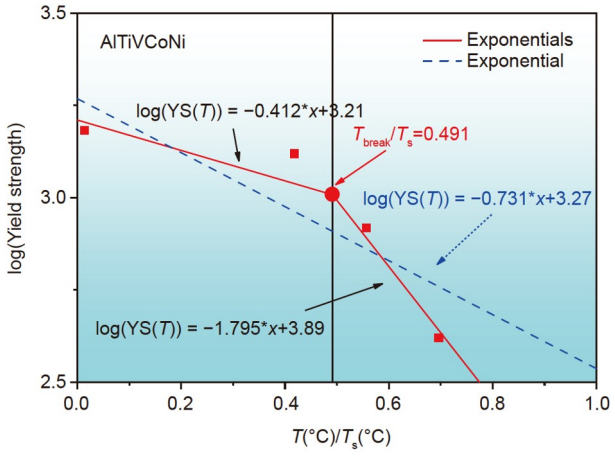

Figure 8 Quantification of the modeling accuracy of the bilinear log model, for the AlTiCoNiV alloy, which compares the modeling accuracy of the bilinear-log model with that of a single exponential model in the semi-logarithmic domain.

The high-temperature softening mechanism of the AlTiVCoNi alloy

To better understand the softening mechanism of the AlTiVCoNi alloy subjected to different high-temperature conditions, EBSD was performed on the compressed samples, and the corresponding images of the long sections are shown in Fig. 10. The results reveal that the grains of the alloy do not change significantly during compression at 600°C, as shown in Fig. 10a. However, at 800 and 1000°C, the alloy undergoes a remarkable dynamic recrystallization softening phenomenon, as presented in Fig. 10b, c. There is an apparent ultrafine equiaxed grain region in the central large deformation region, and plastic-flow deformation occurs in the alloy at 1000°C. More details can be seen in Fig. S5. This trend can also explain the serration flow behaviors on the compression curve.

The enlarged EBSD images of the compressed samples are presented in Fig. 11a, b. It should be mentioned that partially dynamic recrystallization occurs in the alloy at 800°C, and the mixed crystalline region contains both ultrafine (0.5–1 μm) and coarse grains (20–50 μm). This trend is the main reason for the reserved high strength during compression at 800°C. However, complete dynamic-recrystallization occurs in the alloy at 1000°C, where the grains in the dynamic-recrystallization region

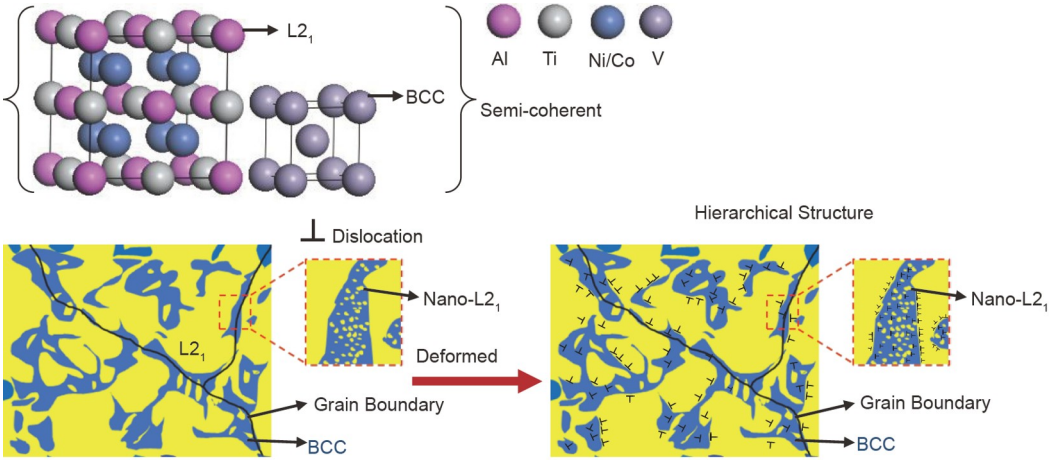

Figure 9 Schematic diagram of the strengthening mechanism *via* the hierarchical structures in the AlTiVCoNi HEA.

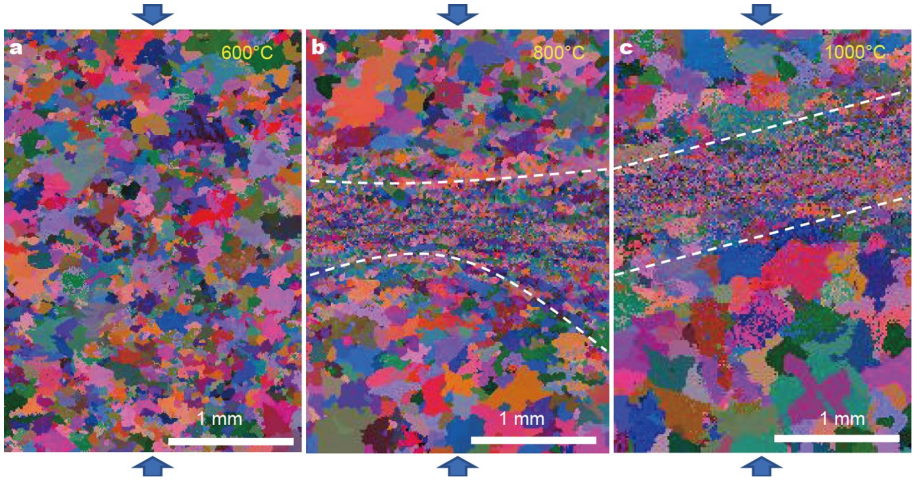

Figure 10 The EBSD all-Euler images of the compressed samples, where the blue arrows indicate the load direction. Here, (a–c) are the samples at 600, 800, and 1000°C, respectively.

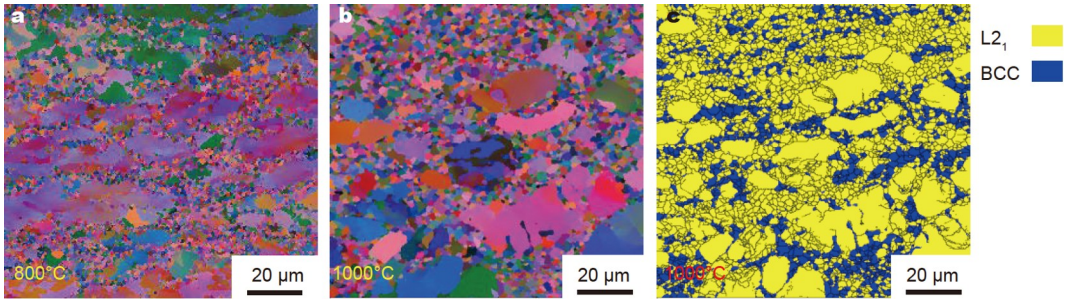

Figure 11 The enlargement of the EBSD all-Euler images of the compressed samples: (a, b) 800 and 1000°C, respectively; (c) the phase map for the sample compressed at 1000°C.

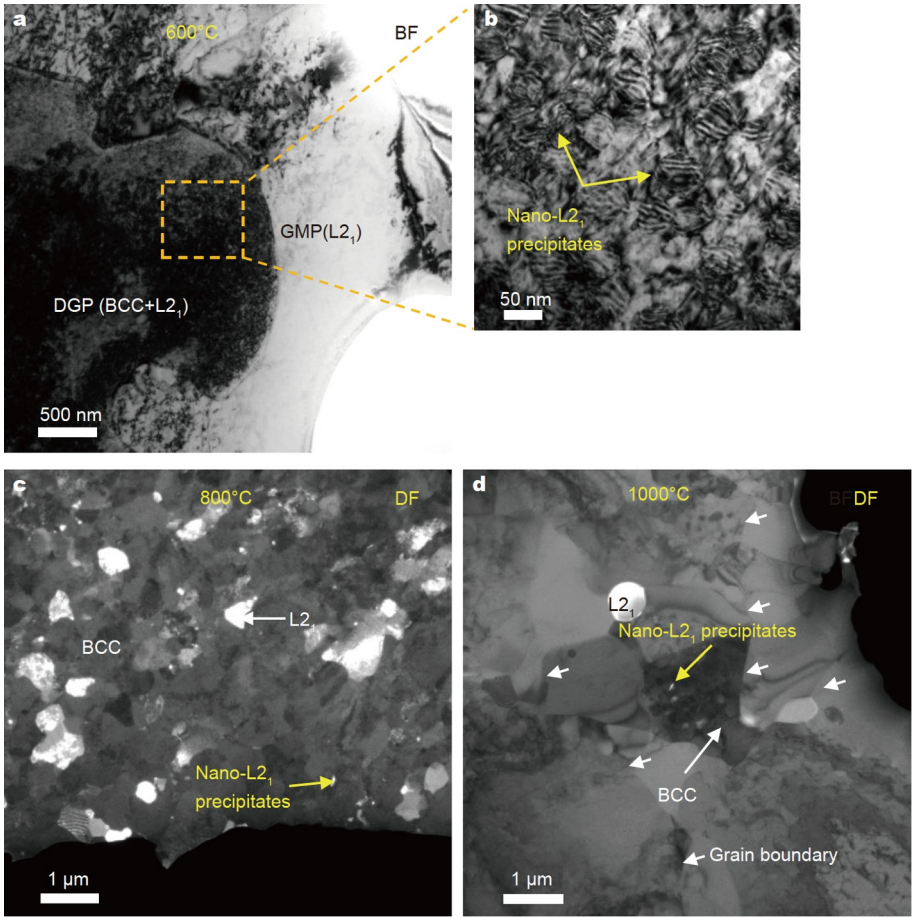

Figure 12 The TEM images of the compressed samples: (a) and (b) correspond to the BF images of the sample at 600°C, while (c) and (d) are the DF images of the samples at 800 and 1000°C, respectively.

grow to relatively large sizes of ~2–5 μm. Fig. 11c shows the phase map of the sample compressed at 1000°C. It can be seen that the recrystallization is mainly concentrated in the interior of the BCC region and near the interface between the BCC and $L2_1$ phases. This result suggests that the BCC phase deforms before the $L2_1$ phase during compression, leading to an increase in the energy density in this region and at the interface between the two phases, which in turn induces dynamic recrystallization. This finding also indicates that in this alloy, the BCC phase is the softer phase that enhances its plasticity, while the $L2_1$ phase is the harder phase that increases its strength. Thus, in the HEAs, this structure and combination of $L2_1$ and BCC phases result in high strength without a significant loss in plasticity. This feature reveals that at 1000°C, the alloy transits into the high-temperature plastic-deformation regime, which is also the primary reason for the high-temperature softening. This phenomenon is consistent with the T_{break} prediction shown in Fig. 8, indicating that the high-temperature softening mechanism of the AlTiCoNiV alloy is the dynamic-recrystallization softening at temperatures above 700°C.

The TEM images of the compressed samples are shown in Fig. 12. Fig. 12a, b correspond to BF images for the sample tested at 600°C. The dislocations are mainly concentrated in the solid-solution DGP area, and some dislocations can also be found at the interface between the GMP and DGP. From the enlarged view of the DGP area in Fig. 12b. As compared with the as-cast

sample, there is no increase in the size of the nano-$L2_1$ precipitates after compression at 600°C. In addition, due to the semi-coherent relationship between the precipitates and the matrix, and the large size of the precipitates (100 nm), the presence of a large amount of nano-$L2_1$ precipitates in the BCC solid solution can hinder dislocation motion through the bypassing mechanism, resulting in their high compressive strength at 600°C. Fig. 12c displays a DF image of the compressed sample at 800°C. There are a large amount of 0.5–1 μm sized dynamic-recrystallization grains of the $L2_1$ and BCC composite in the alloy. Also, there are still some nano-$L2_1$ precipitates that have not increased in size, indicating that dynamic recrystallization occurred. Consequently, there is a decrease in the strength but an increase in the plasticity of the alloy. In addition, the grains in the alloy significantly grow to 2–5 μm under the dynamic recrystallization in the compression process at 1000°C, and most of the nano-$L2_1$ precipitates grow up. There is still a trace of nano-$L2_1$ precipitates in the BCC solid solution, which results in the dramatic reduction of the strength. Lastly, we found that the AlTiVCoNi alloy with the ordered-$L2_1$ + disordered-BCC + nano $L2_1$ hierarchical structure maintains a high strength and plasticity during compression at room temperature and 600°C. The partial dynamic recrystallization occurs during the compression at 800°C, and complete dynamic recrystallization occurs in the strong deformation zone during the compression at 1000°C. Recrystallization results in an increase in the plasticity and an decrease in the strength.

CONCLUSION

In summary, a low-density high-entropy dual-phase AlTiVCoNi alloy with a density of ~6.24 g cm^{-3} was developed. This alloy exhibits a hierarchical structure, and is composed of an ordered-$L2_1$ HEIC phase, a disordered-BCC solid-solution, and nano-$L2_1$ precipitates. It exhibits excellent phase stability after 1200°C + 24 h annealing. Compression testing reveals several important results: the compressive yield strengths of the as-cast and the annealed samples are very close at room temperature (~1.6 GPa); the strength and specific strength of the alloy decrease with the increase of temperature, and it shows an excellent compressive yield strength (~1.3 GPa) and specific yield strength at room temperature and 600°C (~261 and ~210 MPa g^{-1} cm^3, respectively), which is achieved through the hierarchical structure and the semi-coherent relationship between the $L2_1$ and BCC phases. When the deformation temperature is higher than 800°C, the softening mechanism is the dynamic recrystallization in the alloy. It was estimated that the T_{break} of this alloy was ~700°C. Overall, with the help of the ΔS_{mix} and the ΔH_{mix}, it is believed that the composition near the balance point between these two factors will present the interesting microstructure with excellent properties. The development of this semi-coherent ordered and disordered dual-phase hierarchical structure in HEAs provides a new way for designing advanced low-density HEAs with exceptional strengths at both room and elevated temperatures.

Received 6 February 2022; accepted 4 July 2022; published online 29 September 2022

1 Yeh JW, Chen SK, Lin SJ, *et al.* Nanostructured high-entropy alloys with multiple principal elements: Novel alloy design concepts and outcomes. Adv Eng Mater, 2004, 6: 299–303
2 Yao Y, Huang Z, Xie P, *et al.* Carbothermal shock synthesis of high-entropy-alloy nanoparticles. Science, 2018, 359: 1489–1494
3 Lei Z, Liu X, Wu Y, *et al.* Enhanced strength and ductility in a high-entropy alloy *via* ordered oxygen complexes. Nature, 2018, 563: 546–550
4 Shi P, Li R, Li Y, *et al.* Hierarchical crack buffering triples ductility in eutectic herringbone high-entropy alloys. Science, 2021, 373: 912–918
5 Pan Q, Zhang L, Feng R, *et al.* Gradient cell-structured high-entropy alloy with exceptional strength and ductility. Science, 2021, 374: 984–989
6 Lu Y, Huang H, Gao X, *et al.* A promising new class of irradiation tolerant materials: $Ti_2ZrHfV_{0.5}Mo_{0.2}$ high-entropy alloy. J Mater Sci Tech, 2019, 35: 369–373
7 Wu Y, Liaw P, Zhang Y. Preparation of bulk TiZrNbMoV and NbTiAlTaV high-entropy alloys by powder sintering. Metals, 2021, 11: 1748
8 Feng R, Zhang C, Gao MC, *et al.* High-throughput design of high-performance lightweight high-entropy alloys. Nat Commun, 2021, 12: 4329
9 Wang M, Lu Y, Wang T, *et al.* A novel bulk eutectic high-entropy alloy with outstanding as-cast specific yield strengths at elevated temperatures. Scripta Mater, 2021, 204: 114132
10 Varma SK, Sanchez F, Moncayo S, *et al.* Static and cyclic oxidation of Nb-Cr-V-W-Ta high entropy alloy in air from 600 to 1400°C. J Mater Sci Tech, 2020, 38: 189–196
11 Zhang W, Liaw PK, Zhang Y. Science and technology in high-entropy alloys. Sci China Mater, 2018, 61: 2–22
12 Zhang Y, Zuo TT, Tang Z, *et al.* Microstructures and properties of high-entropy alloys. Prog Mater Sci, 2014, 61: 1–93
13 Tsai MH, Yeh JW. High-entropy alloys: A critical review. Mater Res Lett, 2014, 2: 107–123
14 China-Aeronautical-Materials-Handbook-Editorial-Board. China Aeronautical Materials Handbook Second edition -Volume (2). Beijing, China: Standards Press of China, 2001, 874
15 Li R, Gao JC, Fan K. Microstructure and mechanical properties of MgMnAlZnCu high entropy alloy cooling in three conditions. MSF, 2011, 686: 235–241
16 Li R, Gao JC, Fan K. Study to microstructure and mechanical properties of Mg containing high entropy alloys. MSF, 2010, 650: 265–271
17 Yang X, Chen SY, Cotton JD, *et al.* Phase stability of low-density, multiprincipal component alloys containing aluminum, magnesium, and lithium. JOM, 2014, 66: 2009–2020
18 Shao L, Zhang T, Li L, *et al.* A low-cost lightweight entropic alloy with high strength. J Materi Eng Perform, 2018, 27: 6648–6656
19 Li Y, Li R, Zhang Y. Effects of Si addition on microstructure, properties and serration behaviors of lightweight Al-Mg-Zn-Cu medium-entropy alloys. Res Appl Mater Sci, 2019, 1: 13
20 Li R, Wang Z, Guo Z, *et al.* Graded microstructures of Al-Li-Mg-Zn-Cu entropic alloys under supergravity. Sci China Mater, 2019, 62: 736–744
21 Li H, Yang C, Fu J, *et al.* Nano-amorphous-crystalline dual-phase design of $Al_{80}Li_5Mg_5Zn_5Cu_5$ multicomponent alloy. Sci China Mater, 2022, 65: 1671–1678
22 Youssef KM, Zaddach AJ, Niu C, *et al.* A novel low-density, high-hardness, high-entropy alloy with close-packed single-phase nanocrystalline structures. Mater Res Lett, 2015, 3: 95–99
23 Tseng KK, Yang YC, Juan CC, *et al.* A light-weight high-entropy alloy $Al_{20}Be_{20}Fe_{10}Si_{15}Ti_{35}$. Sci China Technol Sci, 2018, 61: 184–188
24 Senkov ON, Wilks GB, Scott JM, *et al.* Mechanical properties of $Nb_{25}Mo_{25}Ta_{25}W_{25}$ and $V_{20}Nb_{20}Mo_{20}Ta_{20}W_{20}$ refractory high entropy alloys. Intermetallics, 2011, 19: 698–706
25 Feng R, Feng B, Gao MC, *et al.* Superior high-temperature strength in a supersaturated refractory high-entropy alloy. Adv Mater, 2021, 33: 2102401
26 Karthick G, Raman L, Murty BS. Phase evolution and mechanical properties of novel nanocrystalline $Y_2(TiZrHfMoV)_2O_7$ high entropy pyrochlore. J Mater Sci Tech, 2021, 82: 214–226
27 Stepanov ND, Shaysultanov DG, Salishchev GA, *et al.* Structure and mechanical properties of a light-weight AlNbTiV high entropy alloy. Mater Lett, 2015, 142: 153–155
28 Stepanov ND, Yurchenko NY, Sokolovsky VS, *et al.* An $AlNbTiVZr_{0.5}$

high-entropy alloy combining high specific strength and good ductility. Mater Lett, 2015, 161: 136–139
29 Xu ZQ, Ma ZL, Wang M, *et al.* Design of novel low-density refractory high entropy alloys for high-temperature applications. Mater Sci Eng-A, 2019, 755: 318–322
30 Qiu Y, Hu YJ, Taylor A, *et al.* A lightweight single-phase AlTiVCr compositionally complex alloy. Acta Mater, 2017, 123: 115–124
31 Qiu Y, Thomas S, Gibson MA, *et al.* Microstructure and corrosion properties of the low-density single-phase compositionally complex alloy AlTiVCr. Corrosion Sci, 2018, 133: 386–396
32 Li Y, Liaw PK, Zhang Y. Microstructures and properties of the low-density $Al_{15}Zr_{40}Ti_{28}Nb_{12}M(Cr,Mo,Si)_5$ high-entropy alloys. Metals, 2022, 12: 496
33 Tan XR, Zhao RF, Ren B, *et al.* Effects of hot pressing temperature on microstructure, hardness and corrosion resistance of $Al_2NbTi_3V_2Zr$ high-entropy alloy. Mater Sci Tech, 2016, 32: 1582–1591
34 Yao H, Liu Y, Sun X, *et al.* Microstructure and mechanical properties of $Ti_3V_2NbAl_xNi_y$ low-density refractory multielement alloys. Intermetallics, 2021, 133: 107187
35 Pang J, Zhang H, Zhang L, *et al.* Ductile $Ti_{1.5}ZrNbAl_{0.3}$ refractory high entropy alloy with high specific strength. Mater Lett, 2021, 290: 129428
36 Senkov ON, Senkova SV, Woodward C, *et al.* Low-density, refractory multi-principal element alloys of the Cr-Nb-Ti-V-Zr system: Microstructure and phase analysis. Acta Mater, 2013, 61: 1545–1557
37 Senkov ON, Senkova SV, Miracle DB, *et al.* Mechanical properties of low-density, refractory multi-principal element alloys of the Cr-Nb-Ti-V-Zr system. Mater Sci Eng-A, 2013, 565: 51–62
38 Feng R, Gao M, Lee C, *et al.* Design of light-weight high-entropy alloys. Entropy, 2016, 18: 333
39 Feng R, Gao MC, Zhang C, *et al.* Phase stability and transformation in a light-weight high-entropy alloy. Acta Mater, 2018, 146: 280–293
40 Xu J, Xia Y, Li Z, *et al.* Multi-physics instrument: Total scattering neutron time-of-flight diffractometer at China Spallation Neutron Source. Nucl Instruments Methods Phys Res Sect A-Accelerators Spectrometers Detectors Associated Equipment, 2021, 1013: 165642
41 Packard JC. Archimedes principle. School Sci Math, 1929, 29: 969–970
42 Yan XH, Liaw PK, Zhang Y. Order and disorder in amorphous and high-entropy materials. Metall Mater Trans A, 2021, 52: 2111–2122
43 Cao P, Ni X, Tian F, *et al. Ab initio* study of $Al_xMoNbTiV$ high-entropy alloys. J Phys-Condens Matter, 2015, 27: 075401
44 Takeuchi A, Inoue A. Classification of bulk metallic glasses by atomic size difference, heat of mixing and period of constituent elements and its application to characterization of the main alloying element. Mater Trans, 2005, 46: 2817–2829
45 Zhang Y, Zhou Y , Lin J , *et al.* Solid-solution phase formation rules for multi-component alloys. Adv Eng Mater, 2008, 10: 534–538
46 Guo S, Ng C, Lu J, *et al.* Effect of valence electron concentration on stability of fcc or bcc phase in high entropy alloys. J Appl Phys, 2011, 109: 103505
47 Yang X, Zhang Y. Prediction of high-entropy stabilized solid-solution in multi-component alloys. Mater Chem Phys, 2012, 132: 233–238
48 Ye YF, Wang Q, Lu J, *et al.* The generalized thermodynamic rule for phase selection in multicomponent alloys. Intermetallics, 2015, 59: 75–80
49 Ye YF, Wang Q, Lu J, *et al.* Design of high entropy alloys: A single-parameter thermodynamic rule. Scripta Mater, 2015, 104: 53–55
50 Nagase T, Rack PD, Noh JH, *et al. In-situ* TEM observation of structural changes in nano-crystalline CoCrCuFeNi multicomponent high-entropy alloy (HEA) under fast electron irradiation by high voltage electron microscopy (HVEM). Intermetallics, 2015, 59: 32–42
51 Yeh JW. Recent progress in high-entropy alloys. Ann Chim Sci Mat, 2006, 31: 633–648
52 Yan X, Zhang Y. Functional properties and promising applications of high entropy alloys. Scripta Mater, 2020, 187: 188–193
53 Yang T, Zhao YL, Tong Y, *et al.* Multicomponent intermetallic nanoparticles and superb mechanical behaviors of complex alloys. Science, 2018, 362: 933–937
54 Lütjering G, Williams JC. Titanium (2nd edition). Berlin, Germany: Springer-Verlag Berlin Heidelberg, 2007, 449
55 Yao K, Liu L, Ren J, *et al.* High-entropy intermetallic compound with ultra-high strength and thermal stability. Scripta Mater, 2021, 194: 113674
56 Zhang Y, Liu JP, Chen SY, *et al.* Serration and noise behaviors in materials. Prog Mater Sci, 2017, 90: 358–460
57 Vegard L. Die konstitution der mischkristalle und die raumfüllung der atome. Z Physik, 1921, 5: 17–26
58 Stepanov ND, Yurchenko NY, Panina ES, *et al.* Precipitation-strengthened refractory $Al_{0.5}CrNbTi_2V_{0.5}$ high entropy alloy. Mater Lett, 2017, 188: 162–164
59 Steingrimsson B, Fan X, Yang X, *et al.* Predicting temperature-dependent ultimate strengths of body-centered-cubic (BCC) high-entropy alloys. npj Comput Mater, 2021, 7: 152
60 Jiang S, Wang H, Wu Y, *et al.* Ultrastrong steel *via* minimal lattice misfit and high-density nanoprecipitation. Nature, 2017, 544: 460–464

Acknowledgements Zhang Y appreciated the supports from the Fundamental Research Funds for the Central Universities (FRF-MP-19-013), Guangdong Basic and Applied Basic Research Foundation (2019B1515120020), the State Key Laboratory for Advanced Metals and Materials, the University of Science and Technology Beijing (2020Z-08), and the Funds for Creative Research Groups of China (51921001). Liao WB thanked the National Natural Science Foundation of China (51801128), and Guangdong Basic and Applied Basic Research Foundation (2021A1515012278 and 2022A1515010288). He Z appreciated the supports from the National Natural Science Foundation of China (51871015 and 52171151). Liaw PK appreciated the supports from the National Science Foundation (DMR-1611180 and 1809640) with program directors, Drs. J. Yang, G. Shiflet, and D. Farkas and the US Army Research Office (W911NF-13-1-0438 and W911NF-19-2-0049) with program managers, Drs. M.P. Bakas, S.N. Mathaudhu, and D.M. Stepp.

Author contributions Li Y conducted the experiments and wrote the draft; Liao WB and Zhang Y conceived the idea and directed the whole project. Chen H, Brechtl J, Song W, Yin W, He Z, and Liaw PK provided valuable suggestions. All authors contributed to the general discussion.

Conflict of interest The authors declare that they have no conflict of interest.

Supplementary information Calculation details and supporting data are available in the online version of the paper.

Yasong Li is a PhD student at the State Key Laboratory for Advanced Metals and Materials, University of Science & Technology Beijing (USTB), under Prof. Yong Zhang's supervision. His research interest is on high-entropy alloys.

Wei-Bing Liao received his PhD degree in materials science and engineering from USTB in 2013. He did post-doctoral work at Peking University from 2013 to 2015, and the City University of Hong Kong from 2015 to 2017. Then, he jointed Shenzhen University as an assistant professor in 2017. His research interest focuses on bulk-metallic glasses and high-entropy alloys.

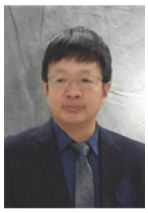

Yong Zhang has been a professor of materials science at the USTB since 2004. He has published over 200 papers and authored a book entitled "High-Entropy Materials, A Brief Introduction" by Springer-Nature publisher. He proposed a parameter to evaluate the configurational entropy effect over the enthalpy effect in the liquid state. It has been verified to be effective in predicting the phase formation for the multicomponent materials.

Peter K. Liaw obtained his BSc degree in physics from Tsing Hua University, Taiwan, and his PhD degree in materials science and engineering from the Northwestern University, in 1980. After working at Westinghouse Research and Development (R&D) Center for thirteen years, he joined the faculty and became an Endowed Ivan Racheff Chair of Excellence at the Department of Materials Science and Engineering, The University of Tennessee (UT), Knoxville in March 1993. He is working in the areas of fatigue, fracture, nondestructive evaluation, and life-prediction methodologies of structural alloys and composites.

一种低密度耐高温高比强度多层次结构双相高熵合金

李亚耸[1], 廖卫兵[2*], 陈怀灿[3], Jamieson Brechtl[4], 宋温丽[3], 殷雯[3], 何占兵[1], Peter K. Liaw[5], 张勇[1,6,7*]

摘要 本文研究了一种新型低密度(~6.24 g cm^{-3})双相AlTiVCoNi高熵合金，其组织结构由有序$L2_1$高熵金属间化合物、无序体心立方结构和纳米$L2_1$相多层次结构构成. 该合金在1200°C + 24 h热处理下未发生相结构转变，在此条件下具有优异的高温相结构稳定性，其铸态和热处理态的压缩屈服强度相当，达到~1.6 GPa. 另外，该合金在室温和600°C条件下表现出了优异的强塑性匹配和优异的比屈服强度，分别达到了约261和210 MPa g^{-1} cm^3. 该合金的超高强度主要源于有序$L2_1$相与体心立方相的半共格界面导致的一种强相结构稳定性和多层次结构的复合强化机制. 该合金在800和1000°C压缩过程中出现了动态再结晶软化，使得其高温强度有所降低. 这种"具有半共格界面$L2_1$ + 体心立方 + 纳米$L2_1$颗粒"的多层次结构设计为开发新型低密度耐高温高熵合金提供了一种新设计思路.